A Theoretical Framework for Aerial Inspection of Siltation in Waterways

Hamza Anwar
Dept. of Electrical Engineering
SBA School of Science & Engineering
LUMS, Pakistan
hmza.anwr@gmail.com

Abubakr Muhammad
Dept. of Electrical Engineering
SBA School of Science & Engineering
LUMS, Pakistan
abubakr@lums.edu.pk

Karsten Berns
Robotics Research Lab
Department of Computer Science
University of Kaiserslautern, Germany
berns@cs.uni-kl.de

***Abstract*—Silt accumulation and sedimentation in canal beds leads to deterioration of watercourses over time. Every year a forced closure of the canals in the Indus basin is inevitable for canal cleaning, entailing a very large scale and costly operation. Silt removal precision is prone to inefficiencies due to subjective decision making in the cleaning process. In this paper, we lay out a theoretical framework to map the semi-structured (emptied) canal bed terrains with an Unmanned Aerial Vehicle (UAV) system for quantitative inspection of deposited silt. The study employs Gaussian process regression on sampled points to determine a continuous distribution of silt surface, thereby, predicting the volume of silt on canal bed. Our theoretical analysis builds upon certain mathematical bounds on the variance of estimated volume, while explicitly considering localization error and sensor noise. Essentially, we setup a framework for studying how tolerable are the process and measurement uncertainties, while achieving a desired accuracy in silt profile and corresponding volume. We demonstrate the regression results in simulations as well as real world lab-scaled-model (LMS151 laser scanner) with different sets of parameters. Volume estimation is verified practically and mathematical performance limits are proposed in established aerial canal inspection system.**

I. Introduction

Inspecting man-made structures or rough outdoor terrains for physical defects, deterioration, usability and safety, involves human inspectors to do safety-critical, expensive and time-consuming engineering tasks. Automating such tasks, has been a hot topic and it has paved way for research developments in aerial, water and ground robotics [10][14][12]. Robotic platforms that can create fast, accurate and detailed 3D models with fused imagery, for inspection of such environments are in progress. All this has led to high-end reliable sensors and precise actuators. However, the need of quantitative analysis of material surfaces inspected along with a theoretical study for maximizing inspection performance, has not been exclusively addressed. Our interest in inspecting and mapping surfaces focuses on maximizing volumetric estimation accuracy of granular media in outdoor terrains for problems like canal cleaning, landscaping, mining, and excavation.

Recently, a lot of work for inspecting safety, productivity and health in infrastructures and industrial facilities has been done with the use of aerial and marine robots. In [21], Corke et al., have proposed control and perception algorithms for pole detection in high frame-rates of a pole inspection UAV system. A similar work by Siegwart et al. is done on the implementation of a flying robot to inspect industrial plant boiler systems [4]. They have concentrated on robust control strategies under real-time constraints for boiler inspection. Researchers in [16] have developed a Micro-Aerial Vehicle (MAV) assistance system for inspecting large naval vessels. Moreover, there is work available on building flight navigation in unstructured environments [2][3]. Others have managed inspection of the environment by physical interaction of MAVs [5][9]. Most of these works address implementation schemes and do not undertake an analysis of the accuracy limits of inferred surfaces.

The civil engineering community has also employed robotic solutions to inspect infrastructure for faults. A group from KAIST [11], has talked about an inspection robot system that attaches itself to a structure and measures the structural displacement in 6-DOF. For bridge inspection, Murphy et al. in [15], have made use of Unmanned Marine Vehicles (UMV). The same group has also developed a UAV-UMV system for littoral environments [19][14] in military applications. Note that, a common factor in these works is the deployment aspect of such field robots. Also these works demonstrate the use of robotic platforms in structural inspection while solving problems of obstacle avoidance, controller design and pose estimation.

In the context of unstructured terrain mapping, we are currently not concerned with navigation. In most works related to outdoor terrains both the aspects are covered together. Due to uneven roughness, navigation and obstacle avoidance become hard problems. For rough terrains, approximating surface maps to planes has been found useful [12][22]. The task of surface estimation reduces to finding a collection of planar surfaces. Although this is an advantage when implementing such systems in field, such studies don't address the rich theoretical analysis that can tell the accuracy limits of estimates. Most importantly, the end objectives of mapping in such applications is acceptable navigation, and not to find the ground truth of encountered terrains.

Most relevant to our current work is research by groups from Carnegie Mellon University [7] and University of Freiburg [13]. In [7], Hebert et al., have argued for a kernel-based learning approach to estimate a continuous surface over the rough terrain to be able to employ a better control in

This work has been funded by LUMS Faculty Initiative Fund (FIF) and German Academic Exchange Service (DAAD) for the project titled *RoPWat* (Robotic Profiling for Clearing Watercourses).

Fig. 1. Examples of bank deterioration (left) and siltation (right) in irrigation canals.

navigation and obstacle avoidance. This prediction also has led to upper and lower bounds on the continuous estimated terrain surface. In [13], Burgard et al., use Gaussian Process regression with non-stationary kernel for accurate terrain modeling of local discontinuity. Their work is further improved and extended in [17]. The key difference between our work and the works mentioned above is that we have explicitly incorporated probabilistic models of robot's localization error and sensor noise in our framework.

The motivation for our work comes from a desire to map the large irrigation canal network in the Indus basin for studying siltation. Water supply to the agricultural base in Pakistan's Indus river basin is through a vast network of irrigation canals that run more than 50,000 km in length. Most of the canals have mud banks and beds which undergo deterioration over time due to accumulation of silt and sediment transported by the rivers. See Fig. 1 for some situations. Every year a forced closure of the canals is inevitable for canal cleaning, entailing a very large scale and costly operation. The extent and precision of silt removal is prone to inefficiencies due to subjective decision making in the cleaning process, shortage of time and lack of verification. The authors aim to develop a semi-autonomous robotic profiling system to increase the efficiency of this process. We propose to develop a 3D perception system, which will be deployed on board an aerial robot to assist the human operator in surveying and subsequently cleaning the canal effectively during the annual canal closures. The current manual system decides on cleaning based on measurements taken every 1000 feet. It looks for at least 6 inch silt depth at these data points. The proposed system envisages efficient cost effective cleaning, reduced water discharge variability, and enhanced agricultural productivity. While a team of roboticists in our respective groups is working on various implementation aspects of the project (algorithms, control, post-processing of acquired data), the aim of this paper is to investigate the achievable performance limits of the proposed aerial canal inspection system in theory.

Our survey shows that there are two distinct areas that connect to the problem we are tackling. On one hand there is work in structural inspection suited for precisely defined environments and on the other there is work on mapping rough uneven surfaces. For our interest, canals offer a semi-structured environment which neither provides a geometric uniformity (like bridges and buildings), nor a relaxation in representation (like fields and forests). Although there is work available on river exploration [10] and other similar tasks, a key point in our work is a probabilistic analysis of how inspection of accumulated silt can improve net performance

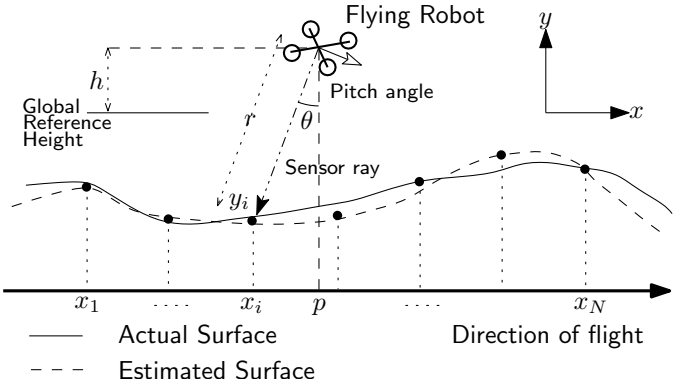

Fig. 2. Side view of a silted canal bed being profiled by a flying robot.

of canal cleaning.

In the past, we have done work on the task of volume estimation of soil by visual inspection algorithms [1]. The goal was to develop a standalone system that measures quantities of any granular material inside a container whose model we acquire separately. We developed a methodology to estimate soil quantities in a bucket excavator, using a stereo vision system. Our approach was to make dense 3D point cloud of the contained material and compare it with an empty container model. Planes were fit over the soil surface using RANdom SAmple Consensus (RANSAC) algorithm, and the difference between the two surfaces was accumulated to give total material volume. Note that, our goal in this paper is not to devise a new algorithm in place of [1], but we aim to determine theoretical bounds on our estimates for canal cleaning application. Moreover, this work incorporates sensor mobility and associated errors, while in [1] the sensor is assumed to be static.

In this paper, we have derived mathematical relationships relating the positioning and sensing uncertainty of robotic inspection vehicles with estimation of the uneven surface profiles and their corresponding enclosed volumes. We setup the canal inspection problem in a basic one-dimensional setting and discuss the sources of uncertainty in robot's localization and sensing. We then regress the scanned surface points into a Gaussian process which gives a mean silt surface surrounded by a confidence interval. Volume encapsulated by this surface is determined by comparing it with previously scanned surface. The mean surface and the confidence interval lead to expressions of scalar mean volume and its variance. We give an analysis of these expressions that essentially show how tolerable are the localization and sensor uncertainties, for achieving a desired accuracy in the profile and corresponding volume estimates. In the end, synthetic lab-scaled experimentation to verify feasibility is presented, whose accurate results strengthen our position in deploying our proposed framework on real large-scale grounds.

II. Problem Setup

Consider a canal that has accumulated silt on its surface, and a flying robot is moving along the dried channel and scanning from above (See Fig. 2). We assume that the canal is dried up and their is no pooling of water with the silted canal bed completely exposed. We've simplified the problem

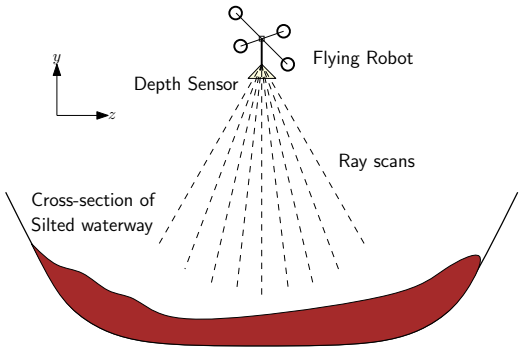

Fig. 3. Cross-sectional view of a silted canal bed profiled by a flying robot.

to a single dimension. The major argument for validity of this simplicity is that we have the canal structure is similar to that of a road. So, we can't measure depth along the channel by taking scans from single point in space, on the contrary, the width of canal is such that the 3D sensor can scan across it in a single scan. In Fig. 3, cross-sectional view of the canal channel is shown with the flying robot scanning the surface. The question of how this problem is simplified to single dimension is addressed by the fact that the robot is moving along the canal and surface fitting is independent along orthogonal axes. In principle, the methods discussed in this paper can be generalized to profile the full 2D canal surface to assess bank deterioration. The sensor mounted on the robot, because of the robot's own localization error, has uncertain position and orientation throughout the operation. Secondly, the sensor also exhibits a noise in its measurements.

The robot's pose vector, $\mathbf{x} = [p \ h \ \theta]^\top$, consists of its position along canal's axis, it's height from level-zero height (desired global mean reference height) and angle tilt in the sensor facing downward. All three variables are independent and distributed normally, and likewise, the range sensor returns are also normally distributed,

$$p \sim \mathcal{N}(\hat{p}, \sigma_p^2), \ \ h \sim \mathcal{N}(0, \sigma_h^2), \ \ \theta \sim \mathcal{N}(0, \sigma_\theta^2), \ \ r \sim \mathcal{N}(\hat{r}, \sigma_r^2).$$

The 2D point on silt surface scanned for each measurement is (x, y). So, we have the following relations,

$$x = p + r\sin\theta, \qquad y = r\cos\theta - h.$$

The resultant distribution for the random variables x and y can be approximated by a gaussian because of its similar density function shape, as shown in Fig. 4. Hence, we can algorithmically, identify the exact values of variances in x and y.

$$x \sim \mathcal{N}(\hat{p}, \sigma_x^2) \qquad y \sim \mathcal{N}(\hat{r}, \sigma_y^2)$$

However, for the scope of this paper, we will approximate $\sigma_x^2 \approx \sigma_p^2$ and $\sigma_y^2 \approx \sigma_r^2$. This is derived from the fact that a practical choice of parameters verifies such an approximation (See Fig. 4). With these sources of uncertainty, an algorithm measures the volume of the silt accumulated on the canal bed. Our goal is to determine theoretical limits on the accuracy we can achieve when we estimate the silt's volume. In determining these bounds, we first need to have a representation of the surface, $f(x)$, from set of scanned points $\{(x_i, y_i)\}_{i=1}^N$, $y_* = f(x_*)$.

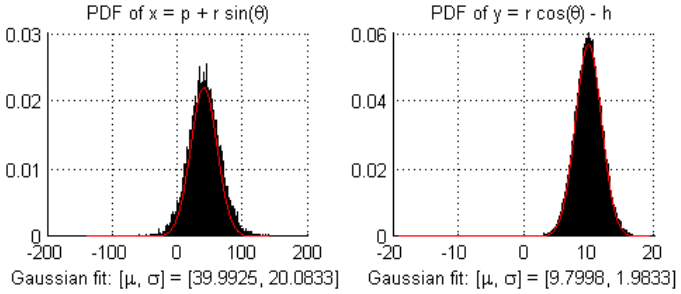

Fig. 4. Black bars show actual density functions of x and y, in left and right figures, respectively. Red curves are best fit Gaussian PDFs. Parameters used: $[\hat{p}, \sigma_p^2, \hat{h}, \sigma_h^2, \hat{r}, \sigma_r^2, \hat{\theta}, \sigma_\theta^2, N] = [40, 20, 0, 0.1, 10, 2, 0, 0.2, 2 \times 10^5]$.

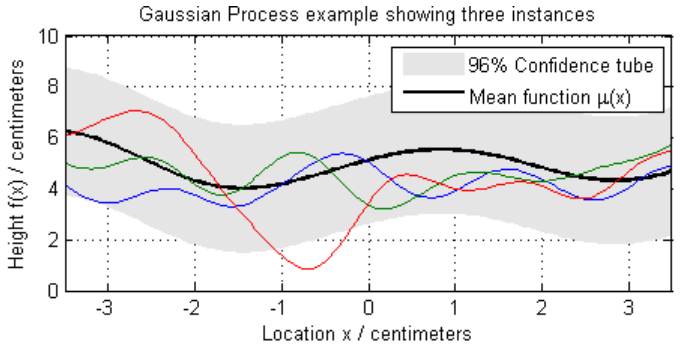

Fig. 5. Textbook example of a Gaussian process showing many instances.

A nice representation, $f(x)$, must have nearby points that are correlated. Beyond a certain resolution details of the surface become unnecessary. Hence, we take the scanned set of points as our landmarks and fit a regression model to get a surface that enforces stronger correlation between nearby points and weaker between points faraway, keeping in mind that it remains smooth and easy to handle.

A. *Estimating the silt surface*

A good candidate for such representation is a Gaussian process. Recall that a Gaussian process is a stochastic process, $f(x)$, for which any finite linear combination of samples has a joint Gaussian distribution. We need two functions i.e. the mean $(\mu(x))$ and covariance functions $(k(x_i, x_j))$ to define $f(x)$.

An example of a Gaussian process is shown in Fig. 5. Here, you have zero mean function, with a squared exponential kernel function (that exhbits exponentially decaying correlation based on distance between points). The figure shows some instances of the process defined by these mean and covariance functions. The key to note here is the smoothness each instance has. Because of other such properties of the squared kernel we have employed the use of Gaussian processes for representing the surface of silt.

B. *Estimating volume of silt*

Once we have an estimate of the silt's surface, we'll determine the mean silt volume and corresponding variance. But first, we'll work out an expression for the integral of a random process. Recall that the mean-square integral of a

random process $f(x)$ over the interval $[-W, W]$ is a random variable, Y_X, defined as the limiting sum given by,

$$Y_X = \int_{-W}^{W} f(x)dx = \lim_{n\to\infty \Delta_k \to 0} \sum_{k=0}^{n-1} f(x_k)\Delta_k.$$

A sufficient condition for mean-square integral, Y_X to exist is that the double integral, $\int_{-W}^{W}\int_{-W}^{W} \mathcal{R}_f(x_1, x_2)dx_1dx_2$, exists. For our case Σ_f, the covariance matrix, exists and it directly relates to $\mathcal{R}_f$, the autocorrelation function, which implies that Y_X will exist.

Since we are considering the one-dimensional case only, we denote the area under the silt's surface as $A = Y_X$. From now on, we will use the terms area and volume interchangeably. We will consider the silt to be defined within $[-W, W]$ which basically are ends of the canal inside robot's view. So, we'll determine the area's mean μ_A and variance σ_A^2:

$$\mu_A = \mathrm{E}[\int f(x)dx] = \int \mathrm{E}[f(x)]dx = \int_{-W}^{W} \mu_f dx,$$

$$\sigma_A^2 = \mathrm{E}[Y_{X_1}Y_{X_2}] = \mathrm{E}[\iint f(x_1)f(x_2)dx_1dx_2],$$

$$= \iint \mathrm{E}[f(x_1)f(x_2)]dx_1dx_2 = \int_{-W}^{W}\int_{-W}^{W} \Sigma_f(x_1, x_2)dx_1dx_2.$$

III. GP Regression: Estimating $f(x)$

In this section we will work out expressions for different cases of the localization error and sensor noise and see how the Gaussian processes regression can help us achieve different surface estimates for the canal's silt. Contents of this section are extracted from [6, p. 51] and [20].

A. No localization error

1) No sensor noise: Firstly, we'll take the completely noise-free base case and later build upon this. In GP regression, we have to initially define a covariance function of our choice, whose parameters would later be learned. So, we chose the squared exponential kernel function because of its wide usage, differentiability and smoothness. Moreover, this kernel function gives us exact solutions even in noisy case.

$$k(x_p, x_q) = ve^{-(x_p - x_q)^2/(2w)}.$$

In determining the the distribution $p(f(x)|x, x_*, y_*)$ where $(x_*, y_*) \in \{(x_i, y_i)\}_{i=1}^N$, since we know that y_* and $f(x)$ are themselves Gaussian distributions, we'd have a joint distribution of y_* and $f(x)$. Then, we'll marginalize out y_* because we already have the training data, to get $f(x)$. So,

$$\begin{bmatrix} y_* \\ f(x) \end{bmatrix} \sim \mathcal{N}\Big(0, \begin{bmatrix} K(x_*, x_*) & K(x_*, x) \\ K(x, x_*) & K(x, x) \end{bmatrix}\Big).$$

Here, $K(x_*, x_*)$ is an $N \times N$ matrix defining covariance of all the training samples. And, similarly $K(x, x)$ denotes covariance matrix of all the test points, and the other two terms are for cross-covariances.

By marginalizing we arrive at following:

$$p(f(x)|x, x_*, y_*) \sim \mathcal{N}(K(x, x_*)(K(x_*, x_*))^{-1}\mathbf{y}_*,$$
$$K(x, x) - K(x, x_*)(K(x_*, x_*))^{-1}K(x_*, x)).$$

y_* is the N dimensional vector of known scanned points. Using simpler notation $\mathbf{k}_* = K(x, x_*) = K(x_*, x)^T$, $K_{xx} = K(x, x)$ and $K = K(x_*, x_*)$, we write it as:

$$p(f(x)|x, x_*, y_*) \sim \mathcal{N}(\mathbf{k}_*^T K^{-1}\mathbf{y}_*, K_{xx} - \mathbf{k}_*^T K^{-1}\mathbf{k}_*).$$

Hence,
$$\mu_f = \mathbf{k}_*^T K^{-1}\mathbf{y}_*,$$
$$\Sigma_f = K_{xx} - \mathbf{k}_*^T K^{-1}\mathbf{k}_*.$$

2) With sensor noise: For a non-zero sensor noise, our scanned points $\mathbf{y}_*$ now have uncertainty. Since we are assuming sensor noise to be uncorrelated between samples so it's effect appears only along the diagonal of the covariance matrix. K changes to $K + \sigma_r^2\mathbf{I}$:

$$\Rightarrow \quad \mu_f = \mathbf{k}_*^T(K + \sigma_r^2\mathbf{I})^{-1}\mathbf{y}_*,$$
$$\Sigma_f = K_{xx} - \mathbf{k}_*^T(K + \sigma_r^2\mathbf{I})^{-1}\mathbf{k}_*.$$

B. With localization error

For the full noisy case, we find that it becomes more complicated. Here, our training data has localization error i.e. $x_i \sim \mathcal{N}(\hat{p}_i, \sigma_{p_i}^2)$. We will see that our kernel function alters because of variance in x_i. By law of iterated expectation:

$$\mathrm{Var}[y_i|\hat{p}_i] = \mathrm{E}_x[\mathrm{Var}[y_i|x_i]] + \mathrm{Var}[\mathrm{E}_x[y_i|x_i]].$$

We take a constant mean prior on $f(x)$ i.e. $\mathrm{Var}[\mathrm{E}_x[y_i|x_i]] = 0$. So,

$$\mathrm{Cov}[y_i, y_j|\hat{p}_i, \hat{p}_j] = \iint \mathrm{Cov}[y_i, y_j|x_i, x_j]p(x_i, x_j)dx_idx_j.$$

Now, we take the assumption that any two random points on the ground from the training data, are independent random variables (i.e. $p(x_i, x_j) = p(x_i)p(x_j)$) and that all have same variance term, $\sigma_{p_i}^2 = \sigma_{p_j}^2 = \sigma_p^2$. So,

$$\Rightarrow k_{\text{noisy}}(\hat{p}_i, \hat{p}_j) = \iint k(x_i, x_j)p(x_i)p(x_j)dx_idx_j,$$

where, $k(x_i, x_j) = \mathrm{Cov}[y_i, y_j|x_i, x_j] = ve^{-(x_i - x_j)^2/(2w)}$. Since our kernel function is squared-exponential, and distribution of x is also Gaussian, we arrive at a product of Gaussians.

$$k_{\text{noisy}}(\hat{p}_i, \hat{p}_j) = \iint \mathcal{N}(0, w)\mathcal{N}(\hat{p}_i, \sigma_p^2)\mathcal{N}(\hat{p}_j, \sigma_p^2)dx_idx_j.$$

Reducing the product of Gaussians and integrating over all x_i and x_j, gives:

$$k_{\text{noisy}}(\hat{p}_i, \hat{p}_j) = v'e^{-(\hat{p}_i - \hat{p}_j)^2/(2w')}. \tag{1}$$

where, $v' = v(1 + 2w\sigma_p^2)^{-1/2}$ and $w' = w + 2\sigma_p^2$. Now, in the end we see that the effect of localization error is a change in the horizontal and vertical length-scales of the covariance

For ease in comparison, we will index the training samples, x_*, as x_i.

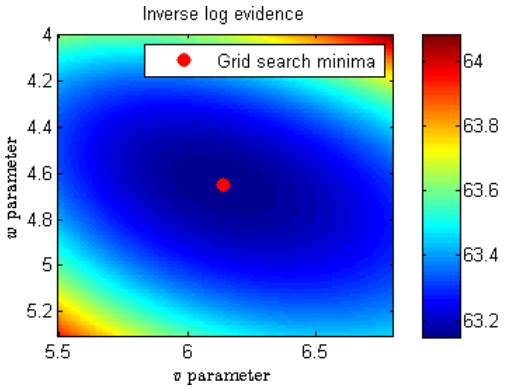

Fig. 6. Model selection for GP regression (brute-force grid-based search for tuning the hyperparameters to fit the data).

function of our Gaussian process, while preserving the shape. We have similar expressions of μ_f and Σ_f with noisy kernel function:

$$\Rightarrow \qquad \mu_f = \mathbf{k}_{*,\text{noisy}}^T (K_{\text{noisy}} + \sigma_r^2 \mathbf{I})^{-1} \mathbf{y}_*,$$
$$\Sigma_f = K_{xx,\text{noisy}} - \mathbf{k}_{*,\text{noisy}}^T (K_{\text{noisy}} + \sigma_r^2 \mathbf{I})^{-1} \mathbf{k}_{*,\text{noisy}}.$$

C. Optimal hyperparameter selection

In order to select best combination of the length scales (i.e. kernel parameters) for regression, we need to maximize the log marginal likelihood:

$$\log p(\mathbf{y}_*|\mathbf{x}_*, v, w) = -\tfrac{1}{2}\mathbf{y}_*(K + \sigma_r^2\mathbf{I})^{-1}\mathbf{y}_* - \tfrac{1}{2}\log|K + \sigma_r^2\mathbf{I}| - \tfrac{n}{2}\log 2\pi$$

Among various methods of maximizing the likelihood, we used grid-based search technique to find a best fit over our acquired data. A large combination of values of v and w were tried and the likelihood was evaluated for each. The combination that maximized the function was chosen as the optimal. Results of which are shown in Fig. 6.

IV. Theoretical bounds on the variance of volume estimate (σ_A^2)

Our goal in this section is to establish certain bounds on σ_A^2 in terms of σ_p^2, σ_r^2 and the process parameters (w and v). Keep in mind the following relations:

$$\Sigma_f(t,s) = K_{xx}(t,s) - \mathbf{k}_*^T(t,s)[K + \sigma_r^2\mathbf{I}]^{-1}\mathbf{k}_*(t,s), \quad (2)$$

$$\sigma_A^2 = \int_{-W}^{W}\int_{-W}^{W} \Sigma_f(t,s)dtds. \quad (3)$$

We will solve the above integral in two parts. Remember that the limits of integration are $[-W, W]$. Firstly, the term $K_{xx}(t,s)$ in (3) has a simple form defined by the kernel function, $k_{\text{noisy}}(t,s)$. This is because K_{xx} is the covariance matrix relating the test points, and since we are estimating the continuous curve $f(x)\ \forall\ x \in \mathbb{R}$, so, $K_{xx}(x_i, x_j)$ comes directly from (1), to be,

$$\iint K_{xx}(t,s)dtds = \iint v' e^{-(t-s)^2/(2w')}dtds,$$

$$= 2v'\Big(w' e^{-2W^2/w'} - w' + W\sqrt{2\pi w'}\,\text{erf}(W\sqrt{\frac{2}{w'}})\Big), \quad (4)$$

where $\text{erf}(x) = \frac{2}{\sqrt{\pi}}\int_0^x e^{-t^2}dt$. Secondly, to find $\iint \mathbf{k}_*^T(t,s)[K + \sigma_r^2\mathbf{I}]^{-1}\mathbf{k}_*(t,s)dtds$, let's first define,

$$H(t,s) := \mathbf{k}_*^T(t,s)[K + \sigma_r^2\mathbf{I}]^{-1}\mathbf{k}_*(t,s).$$

Because of the matrix inversion in the quadratic form, we don't solve this expression explicitly, so we'd use, $H_0(t,s) := \mathbf{k}_*^T(t,s)[\sigma_r^2\mathbf{I}]^{-1}\mathbf{k}_*(t,s)$. Evaluating $\iint H_0(t,s)dtds$ is simpler because $[\sigma_r^2\mathbf{I}]^{-1} = \frac{1}{\sigma_r^2}\mathbf{I}$. So, we can find a closed form expression for it,

$$\iint H_0(t,s)dtds = \iint \sum_{i=1}^{n} \frac{k(a,i)k(b,i)}{\sigma_r^2}dtds.$$

We can interchange integral and summation signs because expression being evaluated is strictly positive valued. This gives us,

$$= \frac{v'^2}{\sigma_r^2}\sum_{i=1}^{n}\iint e^{-((t-x_i)^2+(s-x_i)^2)/(2w')}dtds,$$

$$= \frac{\pi w' v'^2}{2\sigma_r^2}\sum_{i=1}^{n}[\text{erf}\Big(\frac{x_i - W}{\sqrt{2w'}}\Big) - \text{erf}\Big(\frac{x_i + W}{\sqrt{2w'}}\Big)]^2. \quad (5)$$

Now, we will make certain assumptions and highlight key points while avoiding singularities in inversion,

- Sensors are never perfect, i.e. $\sigma_r^2 > 0$.
- Note that, $\mathbf{k}_*(t,s) \geqslant 0\ \forall\ (t,s) \in \mathbb{R}^2$. This pops from the use of squared exponential kernel (1).
- The covariance matrix of training data, K_{xx}, is positive definite, i.e. $K_{xx} \succ 0$, with all individual entries being positive real numbers (choice of kernel).

With these points, we can safely argue that,

$$\mathbf{k}_*^T(K + \sigma_r^2\mathbf{I})^{-1}\mathbf{k}_* \preceq \mathbf{k}_*^T(\sigma_r^2\mathbf{I})^{-1}\mathbf{k}_*,$$

$$\iint \mathbf{k}_*^T[K + \sigma_r^2\mathbf{I}]^{-1}\mathbf{k}_* dtds \leqslant \iint \mathbf{k}_*^T[\sigma_r^2\mathbf{I}]^{-1}\mathbf{k}_* dtds,$$

As a consequence we have,

$$\iint H(t,s)dtds \leqslant \iint H_0(t,s)dtds. \quad (6)$$

Now, from (2) and (3),

$$\sigma_A^2 = \int_{-W}^{W}\int_{-W}^{W} K_{xx}(t,s) - \mathbf{k}_*^T(t,s)[K + \sigma_r^2\mathbf{I}]^{-1}\mathbf{k}_*(t,s)dtds.$$

Using definitions of $H(t,s)$, $H_0(t,s)$ and (6), we construct the inequality,

$$\sigma_A^2 \geqslant \int_{-W}^{W}\int_{-W}^{W} K_{xx}(t,s)dtds - \int_{-W}^{W}\int_{-W}^{W} H_0(t,s)dtds.$$

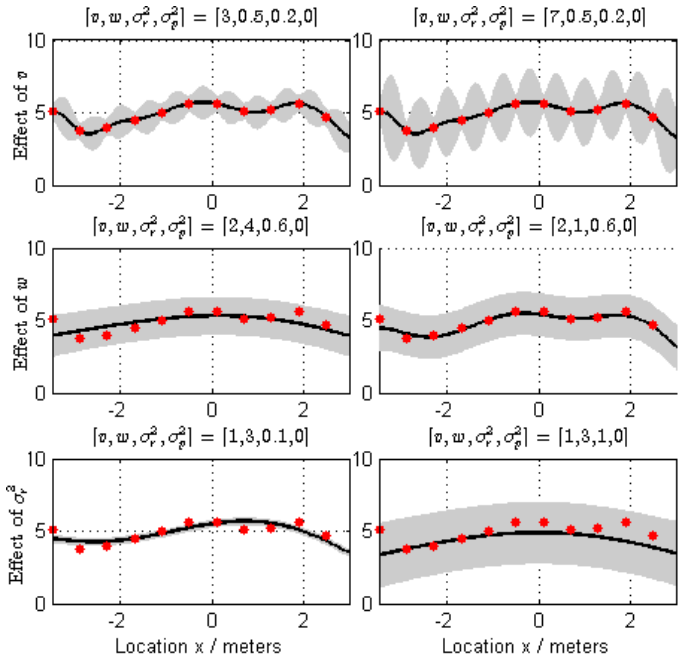

Fig. 7. Posterior of GP regression with different parameter sets showing effects of (v, w, σ_r^2). Red dots are data points, gray region is 96% confidence tube and black curve is the mean.

So, from (4) and (5), our final expression simplifies to,

$$\sigma_A^2 \geqslant 2v'\Big(w'e^{-2W^2/w'} - w' + W\sqrt{2\pi w'}\,\mathrm{erf}(W\sqrt{\frac{2}{w'}})\Big) - \frac{\pi w' v'^2}{2\sigma_r^2}\sum_{i=1}^{n}[\mathrm{erf}\Big(\frac{x_i - W}{\sqrt{2w'}}\Big) - \mathrm{erf}\Big(\frac{x_i + W}{\sqrt{2w'}}\Big)]^2.$$

Note that, since $-1 \leqslant \mathrm{erf}(x) \leqslant 1 \;\forall\; x \in \mathbb{R}$, i.e.

$$\sum_{i=1}^{n}[\mathrm{erf}\Big(\frac{x_i - W}{\sqrt{2w'}}\Big) - \mathrm{erf}\Big(\frac{x_i + W}{\sqrt{2w'}}\Big)]^2 \leqslant 4n, \tag{7}$$

so, a lower bound on the volume variance comes out to be,

$$\sigma_A^2 \geqslant 2v'w'\Big(e^{-2W^2/w'} - 1 - \frac{n\pi v'}{\sigma_r^2} + W\sqrt{\frac{2\pi}{w'}}\,\mathrm{erf}(W\sqrt{\frac{2}{w'}})\Big). \tag{8}$$

One thing we should note that the expression in (7) itself is a measure of dispersion information of the training samples. So, we can look for a tighter bound instead of $4n$ in (7) if we have knowledge about the distribution of samples. But for now, that effect is not deeply analyzed.

V. Simulation Results

We have conducted simulations of this regression technique on our custom dataset. Considering the rough dimensions of the canal and the intended height of flying robot traversing above it, we took the region of interest within robot's view to be -3.5 to 3.5 meters along canal's length ($[-W, W]$). This will act as the side view of the canal (consequently, the x-axis). Secondly, we have numerous parameters of interest like, sensor resolution along robot's position (x-axis), sensor noise in scanned points (along y-axis – σ_r^2), initial guess of horizontal and vertical length scales (i.e. GP parameters – w and v) and most importantly localization error, σ_p^2.

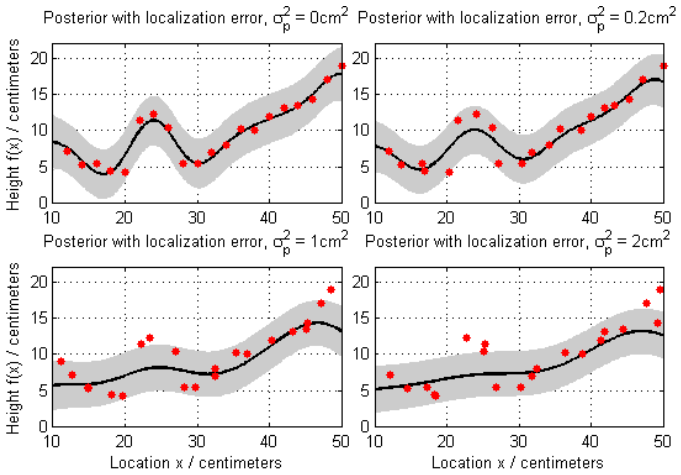

Fig. 8. Regression posterior with changing $\sigma_p^2 = [0, 0.2, 1, 2]$ cm^2. Effect of increasing position error of data points (shown in red) along x-axis is visible.

Depending on the initial choice of the GP parameters (i.e. w and v, recall the kernel function from (1)), we get different estimates of the silt surface, as depicted in Fig. 7. Note that parameters are ordered as $[v, w, \sigma_r^2, \sigma_p^2]$ in all posterior plots. It becomes evident that w controls the smoothness of the estimate, whereas v controls deviation from mean. Likewise, the effect of varying the sensor noise, σ_r^2, on the thickness of the confidence tube is shown in the third row of Fig. 7. An interesting series of experiments performed when we incorporated the localization error in measurements is shown in Fig. 8. Here, we corrupted our data points in both perpendicular axes (sensor noise and localization error) with corresponding normal distributions. For realistic demonstration, we also altered our initial choice of the GP parameters based on their relationships with the variance in localization estimate ($w' = w + 2\sigma_p^2$ and $v' = v(1 + 2w\sigma_p^2)^{-1/2}$).

VI. Experiments on a Scaled Lab Model

A. Surface estimation experiments

After verifying the working of our algorithm to estimate surfaces and their volumes, we tested it for real world data. Our setup consisted of a bucket with 4' × 2' wide mouth filled up with soil (Fig. 9). Sick laser scanner (LMS151) was attached with a prismatic joint to move horizontally over the surface. Progressive scans of the surface were taken by moving the scanner and stopping periodically. The exact position of the scanner along the horizontal axis was noted with the help of an electric potentiometer sensor and a flat ruler. The scan taken at any time gave cross-sectional range data, so enough data was available for constructing a full 3D map of the surface (4' × 2') by moving the scanner along horizontal axis.

We performed four experiments with different types of profiles (Fig. 10). For each experiment we took scans after every 2cm movement of the scanner. Notice that the scanner scans along the cross-section of the channel in one shot (similar to Fig. 3). On each set point (of 2cm) we noted the points at

Fig. 9. Hardware assembly of scaled lab model depicting a scene of a silted canal bed, with a scanner maneuvering above it along length axis. Close-up of LMS151 scanner shown in bottom-left.

Fig. 10. Images of the profiles A, B, C, D (top, right, bottom, left) taken for surface estimation experiment series.

0°(directly facing vertically down, i.e. the central beam of the laser rays) as training points and regressed over them (see the white line chalked in profiles of Fig.10). Each experiment had different set of parameters that optimally fit the surface. These were found out by minimizing the log likelihood as explained in III-C. We assumed zero localization error, and sensor noise variance of $((1.2)^2\text{cm}^2=)\ 1.44\text{cm}^2$ (LMS151) [18]. The reconstructed profiles are shown in Fig. 11.

B. Volume experiment

After surface estimation experiments, we headed towards verifying our algorithm to work with the problem we were actually tackling, that of volume estimation and its bounds. We took the same test bed, made a dig-shaped profile of the soil, Fig.12(a), depicting one possible scene of silted canal channel, and took a scan. Then, we took a cylindrical-shaped object with known dimensions (6.6cm diameter, 15cm length), placed it in the middle of the dig with its length axis perpendicular to the sensor's motion and scanned again, Fig.12(b). After regressing over data points of both the baseline and silted states of the

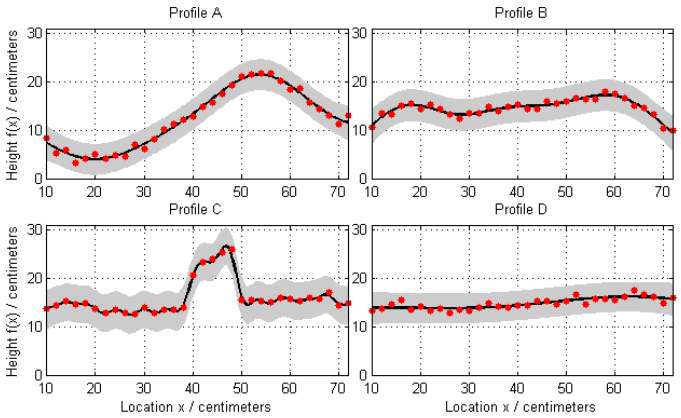

Fig. 11. GP Regression results with optimal parameters of the corresponding profiles (See Fig. 10). Note that, we took $\sigma_r^2 = 1.44\text{cm}^2$ and $\sigma_p^2 = 0$.

Fig. 12. Two states of the channel model for volume experiment: (a) Baseline (left); (b) Silted (right).

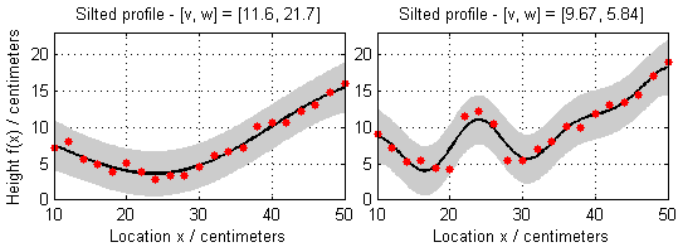

Fig. 13. Corresponding surfaces of the two states of the channel model - Baseline (left) and Silted (right) (See Fig.12). For both, $\sigma_r^2 = 1.44\text{cm}^2$ and $\sigma_p^2 = 0\text{cm}^2$.

channel, independently, with optimized choice of regression parameters, we plotted corresponding profiles 13 and 14. Once we had the two profiles, we overlaid them over each other. We specified our region of interest (i.e. where was had placed our object, between 18cm and 30cm marks) to avoid the error accumulation due to sensor noise, and measured the area of enclosed surface, Fig. 14. The choice of object being cylindrical was to avoid unnecessary surface irregularities about the perpendicular axis. Actual cross-sectional area of the cylinder was $\pi r^2 = 34.22\text{cm}^2$. Estimate given by surface fitting and numerical integration was 40.71cm^2. Moreover, we also determined the variance in the volume estimate, using the approach highlighted in II-B. The standard deviation came out to be 6.423cm^2. The reason for such a high deviation is the high sensor noise (1.44cm^2) and large sampling interval between successive scans (2cm). This concluded our volume experiment with satisfactory results.

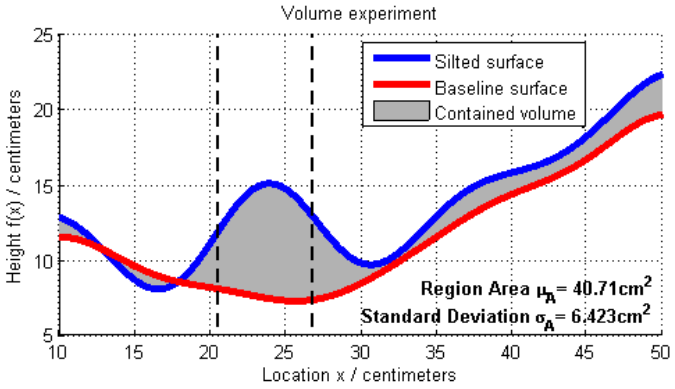

Fig. 14. Plots depicting one-dimensional view of the silt volume estimation experiment. The hump enclosed by the dashed lines represents the approximated surface of the cylindrical object used (See Fig. 12). The difference in surfaces outside this region is because of noise in sensor readings.

VII. Conclusions and Discussion

This paper is a first attempt towards analyzing accuracy of the volume estimates using probabilistic modeling of silt surfaces in canals. Our approach employs Gaussian process regression for modeling surfaces, keeping in mind the uncertainties in robot's localization and its sensor precision. Our novelty lies in incorporating the localization error explicitly and coming up with closed-form expressions that describe limits on the achievable accuracy in silt volume estimate. Simulations have shown the working of our approach and an analysis with various parameters. We have seen that increased localization error can effect the estimation of surface and corresponding silt volume significantly. On the other hand, the sensor noise doesn't alter the shape of estimate dramatically, rather it narrows or tightens the confidence of the estimated mean. Hence, in addition to deploying accurate sensors there is a more pressing need to understand (and improve) the localization capability of the robot for accurate inspection. Series of scaled lab experiments conducted depict feasibility and deployability of our algorithm by expressing accurate surface and volume estimates with variances.

Currently, we have achieved a single lower bound on the volume variance (8). In future, other information related to the dispersion of the data points and sensor resolution can be incorporated to get tighter bounds. Also, a more realistic sensor model (in 3D) can be used for making our results more realistic. We intend to study other kernel functions for regression in this context. The usefulness of our results will become apparent when we are able to compare the performance of manual canal surveying process with that of our aerial inspection system.

Finally, an important aspect in our work is that the focus has not been on developing a new implementable algorithm. Gaussian process regression for large point clouds obtained from 3D sensors may not be practically efficient. However, our analysis provides useful insights before implementing any practical algorithm that hopes to achieve the theoretical performance promised by an optimal estimation framework.

References

[1] H. Anwar, S. M. Abbas, A. Muhammad, and K. Berns, "Volumetric Estimation of Contained Soil using 3D Sensors," *Commercial Vehicle Technology*, pp. 11–13, 2014.

[2] A. Bachrach, R. He, and N. Roy, "Autonomous flight in unknown indoor environments," *International Journal of Micro Air Vehicles*, vol. 1, no. 4, pp. 217–228, 2009.

[3] M. Blosch, S. Weiss, D. Scaramuzza, and R. Siegwart, "Vision based MAV navigation in unknown and unstructured environments," in *Robotics and automation (ICRA), 2010 IEEE international conference on*. IEEE, 2010, pp. 21–28.

[4] M. Burri, J. Nikolic, C. Hurzeler, G. Caprari, and R. Siegwart, "Aerial service robots for visual inspection of thermal power plant boiler systems," in *Applied Robotics for the Power Industry (CARPI), 2012 2nd International Conference on*. IEEE, 2012, pp. 70–75.

[5] G. Darivianakis, K. Alexis, M. Burri, and R. Y. Siegwart, "Hybrid Predictive Control for Aerial Robotic Physical Interaction towards Inspection Operations," in *Proc. of The IEEE International Conference on Robotics and Automation (ICRA)*, 2014.

[6] A. Girard, "Approximate methods for propagation of uncertainty with Gaussian process models," Ph.D. dissertation, University of Glasgow, 2004.

[7] R. Hadsell, J. A. Bagnell, D. F. Huber, and M. Hebert, "Accurate rough terrain estimation with space-carving kernels," in *Robotics: Science and Systems*, vol. 2009. Citeseer, 2009.

[8] C. Hürzeler, "Modeling and design of unmanned rotorcraft systems for contact based inspection," Ph.D. dissertation, ETH Zurich, 2013.

[9] S. Jain, S. Nuske, A. Chambers, L. Yoder, H. Cover, L. Chamberlain, S. Scherer, and S. Singh, "Autonomous River Exploration," in *Proc. of The 9th Intl. Conf. on Field and Service Robots (FSR). Brisbane, Australia*, vol. 5, 2013.

[10] H. Jeon, Y. Bang, and H. Myung, "Structural inspection robot for displacement measurement," in *Digital Ecosystems and Technologies Conference (DEST), 2011 Proceedings of the 5th IEEE International Conference on*. IEEE, 2011, pp. 188–191.

[11] K. Konolige, M. Agrawal, R. C. Bolles, C. Cowan, M. Fischler, and B. Gerkey, "Outdoor mapping and navigation using stereo vision," in *Experimental Robotics*. Springer, 2008, pp. 179–190.

[12] T. Lang, C. Plagemann, and W. Burgard, "Adaptive Non-Stationary Kernel Regression for Terrain Modeling." in *Robotics: Science and Systems*, 2007.

[13] M. Lindemuth, R. Murphy, E. Steimle, W. Armitage, K. Dreger, T. Elliot, M. Hall, D. Kalyadin, J. Kramer, M. Palankar *et al.*, "Sea robot-assisted inspection," *Robotics & Automation Magazine, IEEE*, vol. 18, no. 2, pp. 96–107, 2011.

[14] R. R. Murphy, E. Steimle, M. Hall, M. Lindemuth, D. Trejo, S. Hurlebaus, Z. Medina-Cetina, and D. Slocum, "Robot-assisted bridge inspection," *Journal of Intelligent & Robotic Systems*, vol. 64, no. 1, pp. 77–95, 2011.

[15] A. Ortiz, F. Bonnin-Pascual, and E. Garcia-Fidalgo, "Vessel Inspection: A Micro-Aerial Vehicle-based Approach," *Journal of Intelligent & Robotic Systems*, pp. 1–17, 2013.

[16] C. Plagemann, K. Kersting, and W. Burgard, "Nonstationary Gaussian process regression using point estimates of local smoothness," in *Machine learning and knowledge discovery in databases*. Springer, 2008, pp. 204–219.

[17] F. Pomerleau, A. Breitenmoser, M. Liu, F. Colas, and R. Siegwart, "Noise characterization of depth sensors for surface inspections," in *Applied Robotics for the Power Industry (CARPI)*. IEEE, 2012, pp. 16–21.

[18] K. S. Pratt, R. Murphy, S. Stover, and C. Griffin, "CONOPS and autonomy recommendations for VTOL small unmanned aerial system based on Hurricane Katrina operations," *Journal of Field Robotics*, vol. 26, no. 8, pp. 636–650, 2009.

[19] C. E. Rasmussen and C. K. I. Williams, *Gaussian processes for machine learning*. MIT Press, 2006.

[20] I. Sa, S. Hrabar, and P. Corke, "Outdoor flight testing of a pole inspection UAV incorporating high-speed vision," *Springer Tracts in Advanced Robotics*, 2014.

[21] H. Schäfer, M. Proetzsch, and K. Berns, "Stereo-vision-based obstacle avoidance in rough outdoor terrain," in *International Symposium on Motor Control and Robotics*, 2005.